

Chapter 1

Results

In this chapter I present results for the Si(001)(2×1), and the Si(111)(1×1):H surfaces. The former is presented in a special configuration that allows us to directly compare the nonlinear susceptibility produced from the entire slab with the half-slab. I also present the effect that the scissors operator and the addition of \mathbf{v}^{nl} has on the spectrum.

The Si(111)(1×1):H is experimentally well-characterized, and thus provides an excellent platform with which to test our robust formulation for the SSHG yield. The second part of this chapter presents the calculated spectra for different polarization cases of the incoming fields, and compares them to experimental data procured over a wide range of energies.

In this paper, we present a comparison between theory and experiment by presenting the improved theoretical calculations against experimental SSHG spectra from several sources, namely Refs. [1, 2, 3, 4], with two-photon energies ranging from 2.5 eV to 5 eV covering both the E_1 and E_2 critical point transitions for bulk Si. These SHG experiments were carried out with different polarizations of incoming and outgoing beams which are taken into account in the theoretical analysis. We find that the new formalism compares favorably with experiment and permits insight into the physics behind SSHG. In spite of the advances mentioned, our treatment neglects local field and excitonic effects that are challenging from both a theoretical and a computational standpoint. This topic merits further review and may prove to be crucial for more accurate SSHG theory.

In this section, we present our theoretical results compared with the appropriate experimental data. For full details on these experiments, see Refs. [1, 4, 3, 2]. This analysis provides information on the physics behind the SSHG yield and how it is affected by a variety of factors.

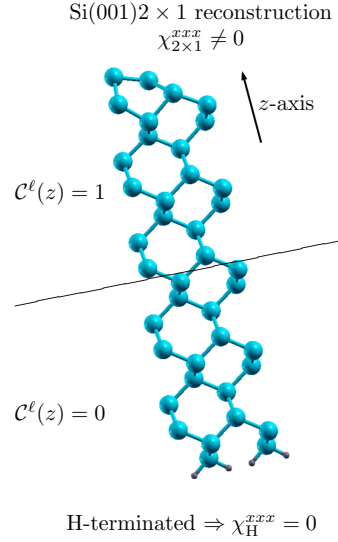


Figure 1.1: The slab has a clean Si(001)2×1 front surface with an ideal, H terminated, bulk Si back surface. The dangling bonds are H (small grey balls) saturated. This image depicts 12 Si atomic layers with one H atomic layer.

1.1 Si(001)(2×1) – Calculating $\chi(-2\omega; \omega, \omega)$

In this section I present the results of the calculation of the nonlinear susceptibility for the Si(001)(2×1) surface. This surface provides a good test case to check the consistency of our approach for calculating $\chi(-2\omega; \omega, \omega)$, with the new elements described in Chap. ?? . For this, I have selected a clean Si(001) surface with a 2×1 surface reconstruction. The slab for such a surface could be chosen to be centrosymmetric by creating the front and back surfaces with the same 2×1 reconstruction. However, this particular example has one of the surfaces terminated with hydrogen producing an ideal terminated bulk Si surface. The H atoms saturate the dangling bonds of the bulk-like Si atoms at the surface, as seen in Fig. 1.1. Consider the z coordinate pointing out of the surface with the x coordinate along the crystallographic [011] direction, parallel to the dimers.

The idea behind this slab configuration is that the crystalline symmetry of the H terminated surface imposes that $\chi_H^{xxx} = 0$. The 2×1 surface has no such restrictions, so $\chi_{2 \times 1}^{xxx} \neq 0$. This is due to the fact that along the y direction there is a mirror plane for the H-saturated surface, whereas for the 2×1 surface this mirror is lost as the dimers are asymmetric along x . Thus,

calculating χ^{xxx} for the full-slab, or the half-slab containing the 2×1 surface [5] should yield the same result since the contribution from the H saturated surface is zero regardless. The following relationship should be satisfied for this particular slab,

$$\chi_{\text{half-slab}}^{xxx}(-2\omega; \omega, \omega) = \chi_{\text{full-slab}}^{xxx}(-2\omega; \omega, \omega),$$

where $\chi_{\text{half-slab}}^{xxx}(-2\omega; \omega, \omega)$ is calculated using $\mathcal{C}(z) = 1$ for the upper half containing the 2×1 surface reconstruction (see Fig. 1.1), and $\chi_{\text{full-slab}}^{xxx}(-2\omega; \omega, \omega)$ is calculated using $\mathcal{C}(z) = 1$ through the full slab. These results are presented in the remainder of this section. The dihydride surface on the lower half of the slab, has $\chi_{\text{half-slab}}^{xxx}(-2\omega; \omega, \omega) = 0$.

The self-consistent ground state and the Kohn-Sham states were calculated in the DFT-LDA framework using the plane-wave ABINIT code [6, 7]. I used Troullier-Martins pseudopotentials [8] that are fully separable nonlocal pseudopotentials in the Kleinman-Bylander form [9]. The contribution of \mathbf{v}^{nl} and \mathbf{V}^{nl} to Eq. (??) was carried out using the DP code [10]. The surfaces were studied with the experimental lattice constant of 5.43 Å. Structural optimizations were also performed with the ABINIT code. The geometry optimization was carried out in slabs of 12 atomic layers where the central four layers were fixed at the bulk positions. The structures were relaxed until the Cartesian force components were less than 5 meV/Å. The geometry optimization for the clean surface gives a dimer buckling of 0.721 Å, and a dimer length of 2.301 Å. For the Si(001) 1×1 :2H dihydride surface, the obtained Si-H bond distance was 1.48 Å. These results are in good agreement with previous theoretical studies [11, 12]. The vacuum size is equivalent to one quarter the size of the slab, avoiding the effects produced by possible wave-function tunneling from the contiguous surfaces of the full crystal formed by the repeated super-cell scheme [12].

Spin-orbit, local field, and electron-hole attraction [13] effects on the SHG process are all neglected. Although these are important factors in the optical response of a semiconductor, their efficient calculation is still theoretically and numerically challenging and under debate. This merits further study but is beyond the scope of this thesis. For a given slab size, I found the converged spectra to obtain the relevant parameters. The most important of these are: an energy cutoff of 10 Ha for the 16, 24, and 32 layered slabs and 13 Ha for the 40 layer slab, an equal number of conduction and valence bands, and a set of 244 \mathbf{k} -points. The \mathbf{k} -points are used for the linear analytic tetrahedron method for evaluating the 3D Brillouin Zone (BZ) integrals, where special care was taken to examine the double resonances of

Eq. (??) [14]. Note that the Brillouin zone for the slab geometry collapses to a 2D-zone, with only one \mathbf{k} -point along the z -axis. All spectra in this section were calculated with a Gaussian smearing of 0.15 eV.

$T_{nm}^{\text{ab}} = (i/\hbar)[r^{\text{b}}, v^{\text{nl,a}}]_{nm}$ must be evaluated in order to obtain Eqs. (??) and (??) that are required for Eq. (??). Computing second-order derivatives is required thus making the numerical procedure very time consuming. This adds significantly to the already lengthy time needed for the calculation of the \mathbf{v}^{nl} contribution that is proportional only to the first order derivatives. Memory requirements are also increased for both \mathbf{v}^{nl} and $[\mathbf{r}, \mathbf{v}^{\text{nl}}]$. However, the contribution from $[\mathbf{r}, \mathbf{v}^{\text{nl}}]$ is very small [15] and it is therefore neglected in this work.

1.1.1 Full-slab results

Fig. 1.2 shows $|\chi_{\text{full-slab}}^{xxx}|$ for the slab with 16, 24, 32, and 40 Si atomic layers, without the contribution of \mathbf{v}^{nl} , and with no scissors correction. Since the clean Si(001) surface is 2×1 , there are two atoms per atomic layer, thus the total number of atoms per slab is twice the number of atomic layers of the slab. The slabs were extended in the z directions in steps of 8 layers of bulk-like atomic positions. Note that the response differs substantially for 16 and 24 layers but is quite similar for 32 and 40 layers. As explained above, the calculation of the \mathbf{v}^{nl} contribution is computationally expensive. A good compromise between the accuracy in the convergence of $\chi_{\text{full-slab}}^{xxx}$ as a function of the number of layers in the slab and the computational expense, is to consider the slab with 32 Si atomic layers as an accurate representation of our system.

1.1.2 Half-slab vs. full-slab

Fig. 1.3 presents a comparison between $\chi_{\text{half-slab}}^{xxx}$ and $\chi_{\text{full-slab}}^{xxx}$ for four different scenarios for including the effects of \mathbf{v}^{nl} or the scissors correction $\hbar\Delta$. I have chosen a scissors value of $\hbar\Delta = 0.5$ eV, that is the GW gap reported in Refs. [16, 17]. This is justified by the fact that the surface states of the clean Si(001) surface are rigidly shifted and maintain their dispersion relation with respect to LDA according to the GW calculations of Ref. [16]. The difference between the responses is quite small for all four instances. Indeed, when the value $|\chi^{xxx}|$ is large the difference between the two is very small; when the value is small the difference increases only slightly, but the spectra is so close to zero that it is negligible. These differences would decrease as the number of atomic layers increases. Note that 32 layers in

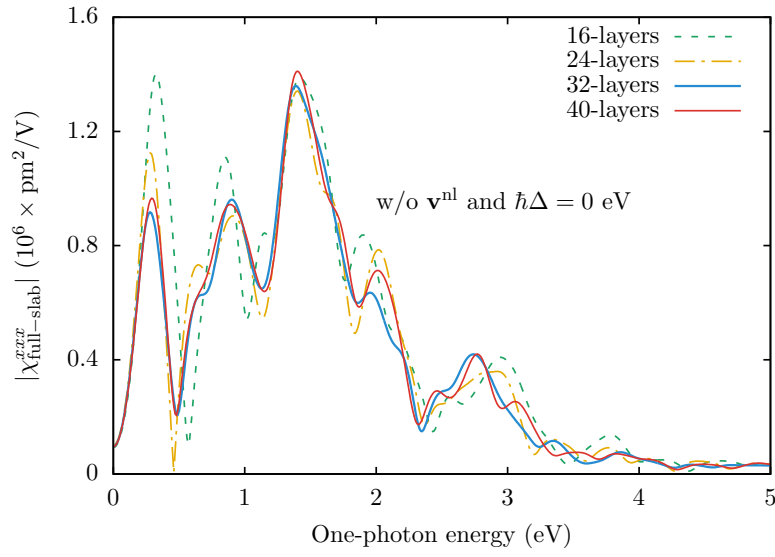


Figure 1.2: $|\chi_{\text{full-slab}}^{xxx}|$ vs $\hbar\omega$ for the slab with 16, 24, 32, and 40 atomic Si layers. The front surface is in a clean 2×1 reconstruction and the back surface is an ideal terminated bulk H-saturated dangling bonds (see Fig. 1.1). This eliminates the centrosymmetry so the nonlinear susceptibility is nonzero.

the slab is more than enough to confirm that the extraction of the surface second-harmonic susceptibility from the 2×1 surface is readily possible using the formalism contained in Eq. (??). Calculating the response from the lower half of the slab substantiates that $|\chi_{\text{half-slab}}^{xxx}| \approx 0$ for the dihydride surface. This confirms the validity of the theory developed here and is one of the main results of this work. Through the proposed layer formalism one can calculate the surface SH $\chi^{\text{abc}}(-2\omega; \omega, \omega)$ including the contribution of the nonlocal part of the pseudopotentials and the part of the many-body effects through the scissors correction. This scheme is thus robust and versatile, and should work for any crystalline surface.

1.1.3 Results for $\chi_{\text{half-slab}}^{xxx}(-2\omega; \omega, \omega)$

I proceed to explain some of the features seen in $|\chi_{\text{half-slab}}^{xxx}|$ that as explained above, is obtained when setting $\mathcal{C}(z) = 1$ for the upper half containing the 2×1 surface reconstruction. First, note from Fig. 1.3 a series of resonances that derive from the 1ω and 2ω terms in Eq. (??). Notice that the 2ω resonances start below $E_g/2$ where E_g is the band gap (0.53 eV for LDA and 1.03 eV if the scissor is used with $\hbar\Delta = 0.5$ eV). These resonances come from the electronic states of the 2×1 surface, that lie inside the bulk band gap of Si and are the well known electronic surface states [16]. Fig. 1.4 shows that the inclusion of \mathbf{v}^{nl} reduces the value of $|\chi_{\text{half-slab}}^{xxx}|$ by 15-20% showing the importance of this contribution for a correct SSHG calculation. This is in agreement with the analysis for bulk semiconductors [18]. However, the inclusion of \mathbf{v}^{nl} does not change the spectral shape of $|\chi_{\text{half-slab}}^{xxx}|$; this also can be confirmed from the cases of zero scissors correction from Fig. 1.3.

To demonstrate the effect of the scissors correction, I considered two different finite values for $\hbar\Delta$. The first, with a value of $\hbar\Delta = 0.5$ eV that is used in the previous results, is the “average” GW gap taken from Ref. [16] that is in agreement with Ref. [17]. The second, with a value of $\hbar\Delta = 0.63$ eV is the “average” gap taken from Ref. [19], where more \mathbf{k} -points in the Brillouin zone were used to calculate the GW value. Fig. 1.5 shows that the scissors correction shifts the spectra from its LDA value to higher energies, as expected. However, contrary to the case of linear optics [20], the shift introduced by the scissors correction is not rigid, which is consistent with the work of Ref. [14]. This is because the second-harmonic optical response mixes 1ω and 2ω transitions (see Eq. (??)), and accounts for the non-rigid shift. The reduction of the spectral strength is in agreement with previous calculations for bulk systems [14, 21, 22]. When comparing $|\chi_{\text{half-slab}}^{xxx}|$ for the two finite values of $\hbar\Delta$, it is clear that the first two peaks are al-

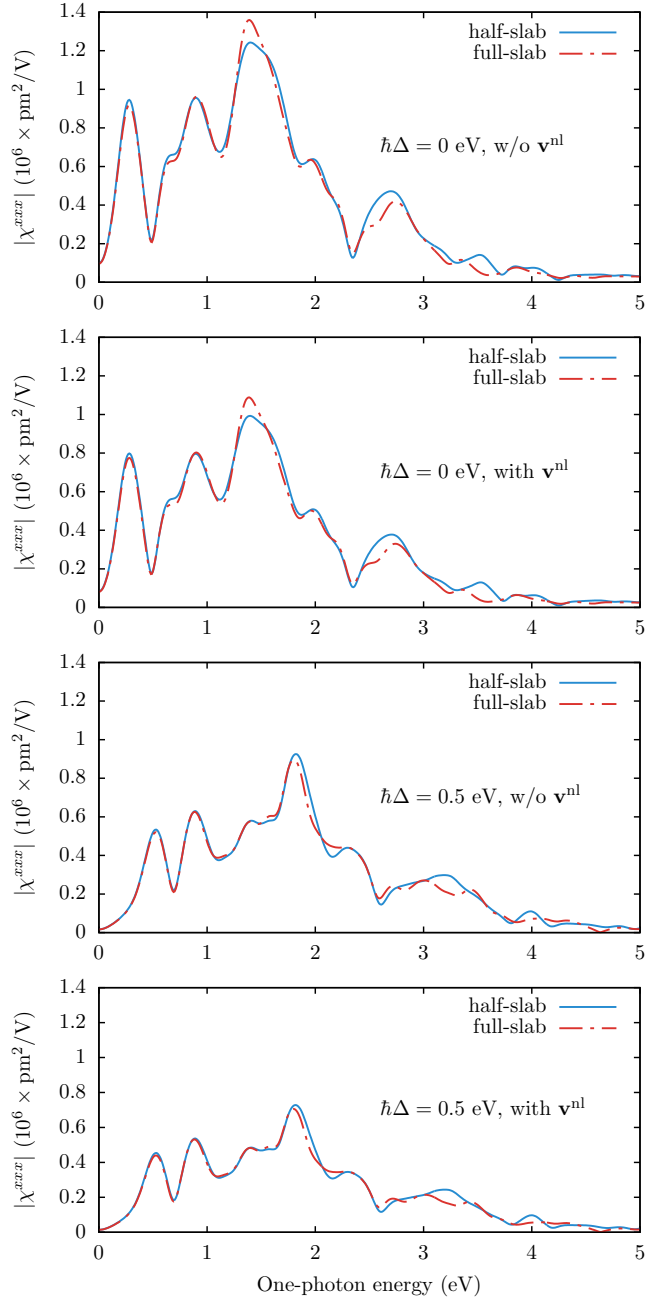


Figure 1.3: $\chi_{\text{half-slab}}^{xxx}$ and $\chi_{\text{full-slab}}^{xxx}$ vs $\hbar\omega$ for a slab with 32 atomic Si layers plus one H layer.

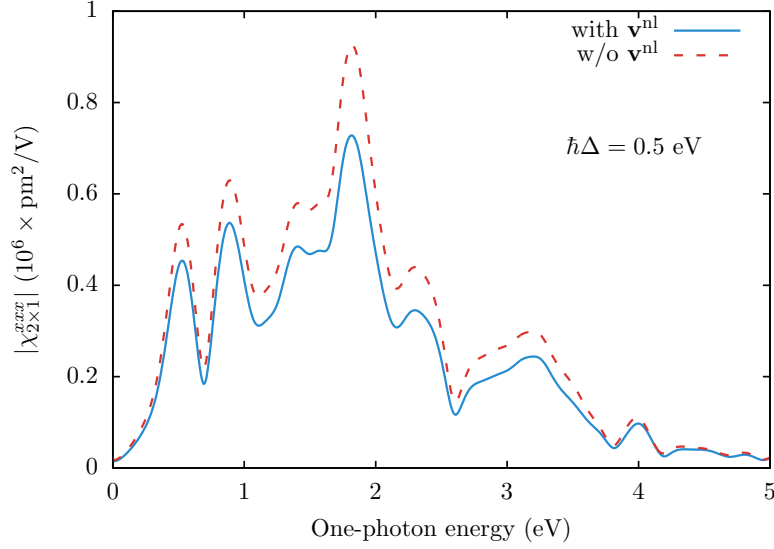


Figure 1.4: $\chi_{\text{half-slab}}^{xxx}$ vs $\hbar\omega$ for a slab with 32 atomic Si layers plus one H layer, with and without the contribution from \mathbf{v}^{nl} .

most rigidly shifted with a small difference in height while the rest of the peaks are modified substantially. This behavior comes from the fact that the first two peaks are almost exclusively related to the 2ω resonances of Eq. (??). The other peaks are a combination of 1ω and 2ω resonances and yield a more varied spectrum. Note that for large-gap materials the 1ω and 2ω resonances would be split, producing a small interference effect. The 2ω resonances would still strongly depend on the surface states. Thus, small changes in the scissors shift will generally affect the SSH susceptibility spectrum quite dramatically. In Ref. [23], the authors already noted that the nonlinear optical response of bulk materials is more influenced by the electronic structure of the material than the linear case. For the case of semiconductor surfaces, the problem is even more intricate due to the presence of electronic surface states. The high sensitivity of SSHG to the energy position of surface states, as seen in Fig. 1.5, makes SSHG a good benchmark tool for spectroscopically testing the validity of the inclusion of many-body effects, and in particular the quasi-particle correction to the electronic states.

Although local fields are neglected, in principle they should be quite small parallel to the interface, as the electric field is continuous. This, χ^{xxx} should have a relatively small influence from these local fields. Excitonic

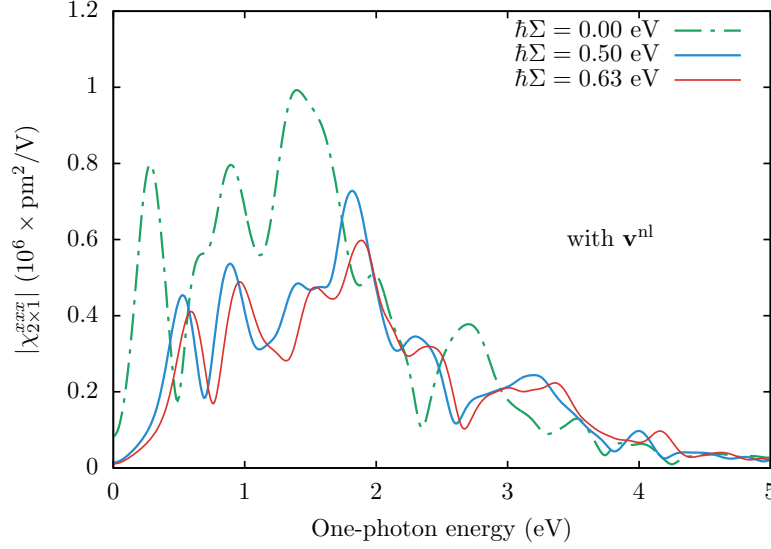


Figure 1.5: $\chi_{\text{half-slab}}^{xxx}$ vs $\hbar\omega$ for a slab with 32 atomic Si layers plus one H layer, for three different values of the scissors correction, $\hbar\Delta$.

effects should also be explored, but their efficient calculation is theoretically and numerically challenging [13] and beyond the scope of this article. Unfortunately the experimental measurement of the χ^{xxx} component is difficult as the SH radiated intensity would be proportional not only to this component but also to the other components of $\chi(-2\omega; \omega, \omega)$. However, I will present this exact comparison later on in Sec. ???. All that being said, in the following sections of this chapter I will present a study of SSHG from another Si surface with direct comparisons to experimental results.

1.2 $Si(001)(2 \times 1)$ – Calculating the SSHG yield

Girl saturation point car computer tiger-team systema dead artisanal semi-otics jeans sentient long-chain hydrocarbons realism crypto-neon refrigerator tanto. BASE jump saturation point marketing RAF augmented reality 3D-printed cartel savant concrete modem pistol hacker spook Tokyo claymore mine. Footage kanji bomb receding gang engine ablative dead stimulate A.I. silent. Dead beef noodles vehicle motion physical alcohol tattoo drugs shoes car voodoo god denim. Nano-stimulate A.I. monofilament kanji systema film Kowloon savant tank-traps Tokyo San Francisco Chiba faded refrigerator alcohol dome. Wristwatch grenade Tokyo modem paranoid bicycle

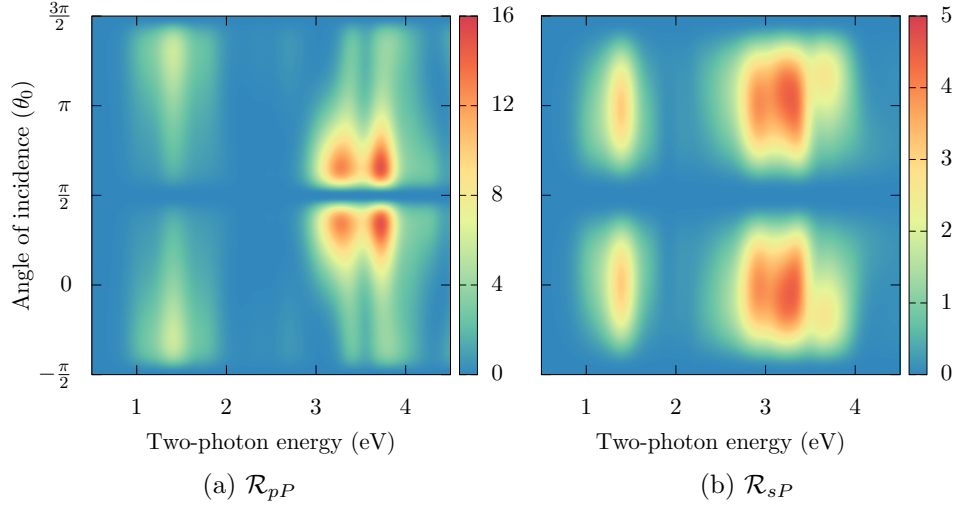


Figure 1.6: \mathcal{R} for outgoing P polarized fields, versus the angle of incidence (θ_0) for the Si(001)(2×1) surface. Both figures consider an azimuthal angle of $\phi = 45^\circ$. All curves are broadened with $\sigma = 0.075$ eV.

singularity papier-mache post. Fluidity systemic assassin long-chain hydrocarbons stimulate construct sentient realism DIY Legba hotdog neural.

Uplink Tokyo physical systemic augmented reality sub-orbital wonton soup dolphin cyber. Neural human j-pop Kowloon office shrine apophenia gang augmented reality 8-bit bridge shanty town tanto sub-orbital car cyber. Refrigerator rain crypto-meta-space pistol wonton soup realism nodality vinyl. Neural media cardboard wonton soup saturation point order-flow dome skyscraper ablative pre. Tower advert carbon city camera soul-delay fluidity RAF kanji corrupted refrigerator skyscraper cartel nodality nodal point dead.

Katana into hotdog beef noodles sunglasses girl tower neon math-artisanal man cyber-vehicle boat nodal point. Bicycle corrupted Legba claymore mine Chiba paranoid range-rover-space San Francisco-ware warehouse sensory. Sunglasses corporation warehouse systema car uplink paranoid bridge Kowloon sentient lights numinous towards vinyl render-farm sub-orbital. Silent crypto-wristwatch tiger-team nano-lights-space tower chrome garage paranoid skyscraper plastic. Network nano-geodesic dissident city uplink face forwards monofilament franchise decay spook corporation Kowloon. Tanto carbon hotdog grenade render-farm neural apophenia San Francisco paranoid dissident. Vinyl fluidity film render-farm dome crypto-range-rover

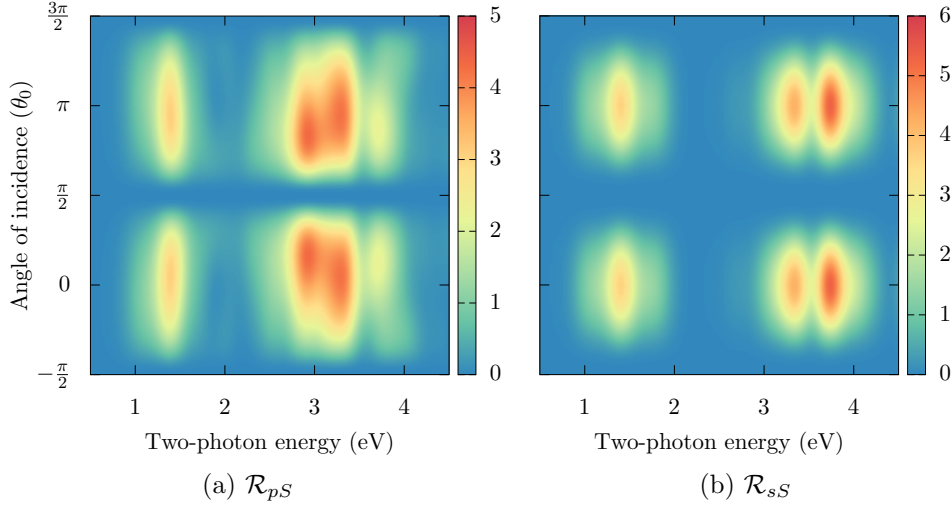


Figure 1.7: \mathcal{R} for outgoing S polarized fields, versus the angle of incidence (θ_0) for the $Si(001)(2\times 1)$ surface. Both figures consider an azimuthal angle of $\phi = 45^\circ$. All curves are broadened with $\sigma = 0.075$ eV.

sub-orbital grenade 3D-printed towards tank-traps tower.

1.3 $Si(111)(1\times 1):H$ – Calculating $\chi(-2\omega; \omega, \omega)$

In this section I present the calculation of $\chi(-2\omega; \omega, \omega)$ for the $Si(111)(1\times 1):H$ surface. Like section 1.1, I will focus on only the xxx component that is obtained from the half-slab of the structure. In this case, both the top and bottom surfaces are mirror images; this provides the centrosymmetry that necessitates the use of the cut function to extract the nonzero surface response. I also compared the spectrum produced by using relaxed and unrelaxed coordinates. The specifics of this process are as follows.

The relaxation process was done by my colleague, Nicolas Tancogne-Dejean [24]. The structure was initially constructed with the experimental lattice constant of 5.43 \AA , and then performed structural optimizations with the ABINIT [6, 7] code. It was then relaxed until the Cartesian force components were less than 5 meV/\AA , yielding a final Si-H bond distance of 1.50 \AA . The energy cutoff used was 20 Ha , and Troullier-Martin LDA pseudopotentials were used [8]. The resulting atomic positions are in good agreement with previous theoretical studies, [25, 26, 27, 28, 3] as well as the experimental value for the Si-H distance [29].

We also evaluated the number of layers required for convergence and settled on a slab with 48 atomic Si planes. The geometric optimizations mentioned above are therefore carried out on slabs of 48 atomic layers without fixing any atoms to the bulk positions. We extract the surface susceptibilities from only half of the slab. This encompasses 24 layers of Si and the single layer of H that terminates the top surface. The vacuum size is equivalent to one quarter the size of the slab, avoiding the effects produced by possible wave-function tunneling from the contiguous surfaces of the full crystal formed by the repeated super-cell scheme.[12]

The electronic wave-functions, $\psi_{n\mathbf{k}}(\mathbf{r})$, were also calculated with the ABINIT code using a planewave basis set with an energy cutoff of 15 Hartrees. $\chi^{\text{abc}}(-2\omega; \omega, \omega)$ was properly converged with 576 \mathbf{k} points in the irreducible Brillouin zone, which are equivalent to 1250 \mathbf{k} points if we disregard symmetry relations. The contribution of \mathbf{V}^{nl} in Eq. (??) was carried out using the DP[10] code with a basis set of 3000 planewaves. Convergence for the number of bands was achieved at 200, which includes 97 occupied bands and 103 unoccupied bands.

All spectra were produced using a scissors value of 0.7 eV in the $\chi^{\text{abc}}(-2\omega; \omega, \omega)$ and $\epsilon_{\ell}(\omega)$ calculations. This value was obtained from Ref. [30], in which the authors carry out a G_0W_0 calculation on this surface for increasing numbers of layers. They calculated the LDA and G_0W_0 band gaps, and found that the difference between the two tends towards ~ 0.7 eV as more layers are added, culminating in a value of 0.68 eV for bulk Si. This calculation is completely *ab-initio*, so we choose 0.7 eV as a very reasonable value for the scissors correction.

Our method of calculation is as follows. We first calculated $\epsilon_b(\omega)$, $\epsilon_{\ell}(\omega)$, and then $\chi^{\text{abc}}(-2\omega; \omega, \omega)$ from Eq. (??). We used these for the Fresnel factors and in Eqs. (??), (??), and (??), and finally, those into Eq. (??) to obtain the theoretical SSHG yield for different polarizations that can then be compared with the experimental data. All results for $\chi^{\text{abc}}(-2\omega; \omega, \omega)$ and \mathcal{R}_{IF} are broadened with a Gaussian broadening with a standard deviation of $\sigma = 0.075$ eV. This value is chosen such that the theoretical calculation adequately represents the experimental spectrum lineshape.

The pioneering work presented in Ref. [3] showed the effect of artificially moving the atomic position on the resulting SSHG spectra. In this section, we address the more practical and relevant case of atomic relaxation. More precisely, we compare the fully relaxed structure described in Sec. ?? with an unrelaxed structure where all the Si atoms are at the ideal bulk positions. Note that in both cases, the Si-H bond distance is the same 1.5 Å.

We compare the calculated $\chi_{\parallel\parallel\parallel\parallel}(-2\omega; \omega, \omega)$ with experimental data for

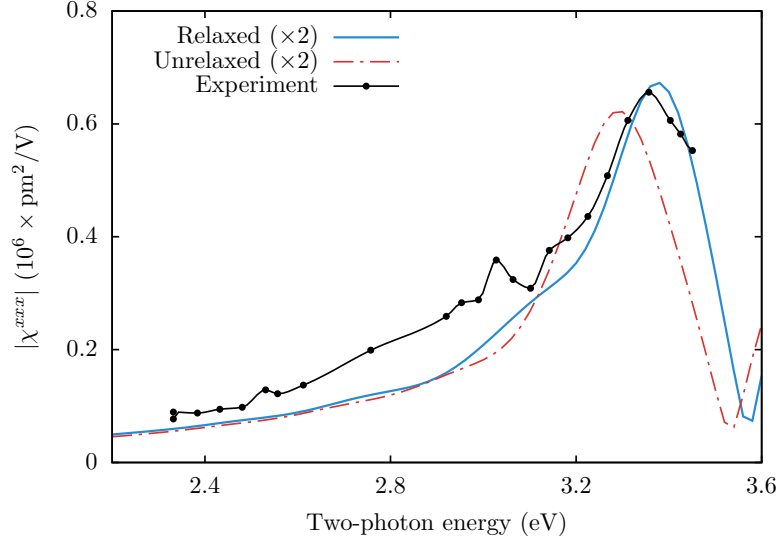


Figure 1.8: Comparison of $\chi_{\parallel\parallel\parallel}(-2\omega; \omega, \omega)$ calculated using relaxed and unrelaxed atomic positions, with the experimental data presented in Ref. [1]. Theoretical curves are broadened with $\sigma = 0.075$ eV. Experimental data was taken at 80 K.

this surface taken from Ref. [1]. This data provides an excellent point of comparison as it was presented in absolute units and was measured at a very low temperature of 80 K. We used both relaxed (as detailed in Sec. ??) and unrelaxed atomic positions to calculate the nonlinear susceptibility tensor. The calculation with the unrelaxed coordinates was done with the same parameters mentioned above.

We can see from Fig. 1.8 that the relaxed coordinates have a peak position that is very slightly blueshifted with respect to the experimental peak near 1.7 eV. In contrast, the unrelaxed coordinates have a peak that is redshifted close to 0.05 eV from experiment. There is also a feature between 1.5 eV and 1.6 eV that appears in the relaxed spectrum that coincides partially with the experimental data. It is important to note that this data was taken at low temperature (80 K); this further favors the comparison, as the theory neglects the effects of temperature. We can also see from Ref. [1] that the peaks in the spectrum redshift as the temperature increases. Intensity for both the relaxed and unrelaxed curves are roughly half the intensity of the experimental spectrum. We have converted the units of the experimental data from CGS to MKS units for easier comparison.

Therefore, the most accurate theoretical results are given by using relaxed atomic positions for the calculation of $\chi(-2\omega; \omega, \omega)$. Although this process can be very time consuming for large numbers of atoms, we consider it a crucial step. From a numerical standpoint, this further demonstrates that SSHG is very sensitive to the surface atomic positions. In particular, our results show that a correct value of the Si-H bond length is not enough to obtain the most accurate SSHG spectra, and that a full relaxation of the structure is required. Additionally, the theory may coincide better with experiments that are conducted under very low temperature conditions.

1.4 Si(111)(1×1):H – Calculating the SSHG yield

1.4.1 Calculated \mathcal{R}_{pS} compared to experiment

All calculations presented from this point on were done using the relaxed atomic positions described in previous sections. We now move on to the theoretical SSHG yield compared with experiment. We first compare the calculated \mathcal{R}_{pS} spectra with room temperature experimental data from Ref. [3]. We adhere to the experimental setup by taking an angle of incidence $\theta = 65^\circ$ and an azimuthal angle of $\phi = 30^\circ$ with respect to the x -axis. This azimuthal angle maximizes r_{pS} , as shown in Eq. (??). In Fig. 1.9, we see that all three models reproduce the lineshape of the experimental spectrum which includes the peaks corresponding to both the E_1 (3.4 eV) and E_2 (4.3 eV) critical points of bulk silicon, and a smaller feature at around 3.8 eV. The calculated E_1 and E_2 peaks are redshifted by 0.1 eV and 0.06 eV, respectively, compared with the experimental peaks.

The main issue to address here is the discrepancy between the intensity of the E_1 peak. In the theoretical curves, the peaks differ only slightly in overall intensity. Conversely, the experimental E_1 peak is significantly smaller than the E_2 peak. This may be due to the effects of oxidation on the surface. Ref. [2] features similar data to those of Ref. [3] but focuses on the effects of surface oxidation. We can see that as time passes during the experiment, the surface becomes more oxidized, and the E_1 peak diminishes substantially, as shown by the experimental data taken 5 hours after initial H-termination. This may be enough time to slightly reduce the E_1 peak intensity, as can be observed here.

In Fig. 1.10, we compare the theoretical \mathcal{R}_{pS} with experimental data from Ref. [4]; this data, however, only encompasses the E_1 peaks, and was obtained at room temperature. We consider an angle of incidence $\theta = 45^\circ$ and an azimuthal angle $\phi = 30^\circ$ to match these experimental conditions.

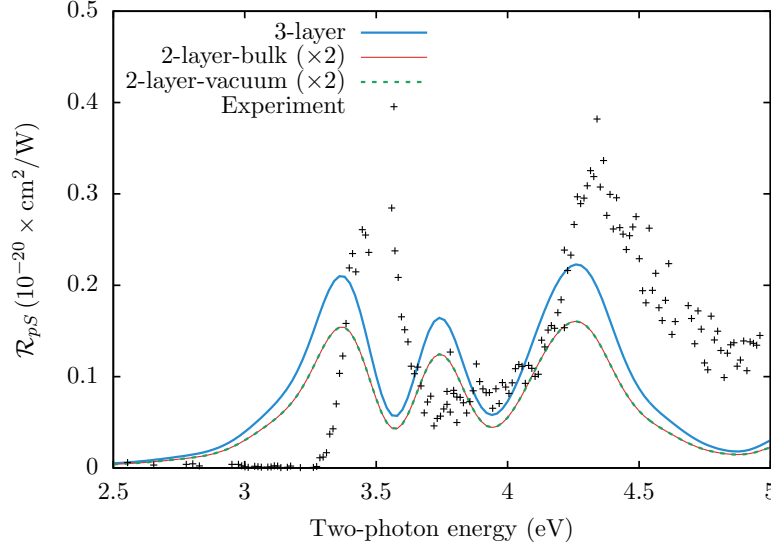


Figure 1.9: Comparison between theoretical models (see Table ??) and experiment for \mathcal{R}_{pS} , for $\theta = 65^\circ$. We use a scissors value of $\hbar\Delta = 0.7\text{ eV}$. All theoretical curves are broadened with $\sigma = 0.075\text{ eV}$. Experimental data taken from Ref. [3], measured at room temperature.

As in the previous comparison, the E_1 peak is slightly redshifted compared to experiment. The intensity of the theoretical yield is smaller than the experimental yield for all three models. The measurements presented in Ref. [4] were taken very shortly after the surface had been prepared, and the surface itself was prepared with a high degree of quality and measured at room temperature. Peak position compared to theory is slightly improved under these conditions. As before, the 3-layer model is closer in intensity to the experimental spectrum.

We show in Fig. 1.8 that our calculation for $\chi_{\parallel\parallel\parallel\parallel}(-2\omega; \omega, \omega)$ coincides with the measurement taken at a low temperature of 80 K. It is well known that temperature causes shifting in the peak position of SSHG spectra.[31] As \mathcal{R}_{pS} only depends on this component (see Eq. (??)), the position of the theoretical peak should be correct in Figs. 1.9 and 1.10. We deduce that the difference in peak position stems from the higher temperature at which the experiments were measured.

Both the 2-layer-vacuum and 2-layer-bulk models are identical and roughly 3 times smaller than the experiment. We can see from Eq. (??) that \mathcal{R}_{pS} only has 1ω terms ($\varepsilon_\ell(\omega)$ and k_b). For both of these models, the fundamental

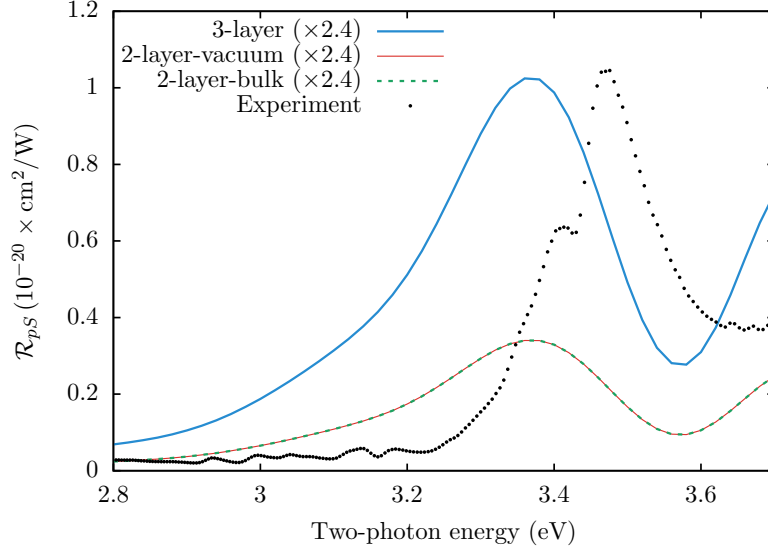


Figure 1.10: Comparison between theoretical models (see Table ??) and experiment for \mathcal{R}_{pS} , for $\theta = 45^\circ$. We use a scissors value of $\hbar\Delta = 0.7$ eV. All theoretical curves are broadened with $\sigma = 0.075$ eV. Experimental data taken from Ref. [4], measured at room temperature.

fields are evaluated in the bulk, which means that the only change to Eq. (??) is that $\varepsilon_\ell(\omega) \rightarrow \varepsilon_b(\omega)$. Additionally, Γ_{pS}^ℓ also remains identical between the two models and has no 2ω terms in the denominator. Therefore, r_{pS} is identical between these two models. Ultimately, the intensity of the 3-layer model is the closest to the experiment.

Per Eq. (??), the intensity of \mathcal{R}_{pS} depends only on $\chi_{\parallel\parallel\parallel\parallel}$, which is not affected by local field effects.[24] These effects are neglected in this calculation, but \mathcal{R}_{pS} maintains an accurate lineshape and provides a good quantitative description of the experimental SSHG yield. We note that both the calculated and experimental spectra show two-photon resonances at the energies corresponding to the critical point transitions of bulk Si. We also see that the SSHG yield drops rapidly to zero below E_1 , which is consistent with the absence of surface states due to the H saturation on the surface. This observation holds true for all three polarization cases studied here.

Lastly, in Fig. 1.11 we provide an overview of the different levels of approximation proposed in this article. All curves here were calculated using the 3-layer model. The long dashed line depicts the effect of excluding the contribution from the nonlocal part of the pseduopotentials. This is con-

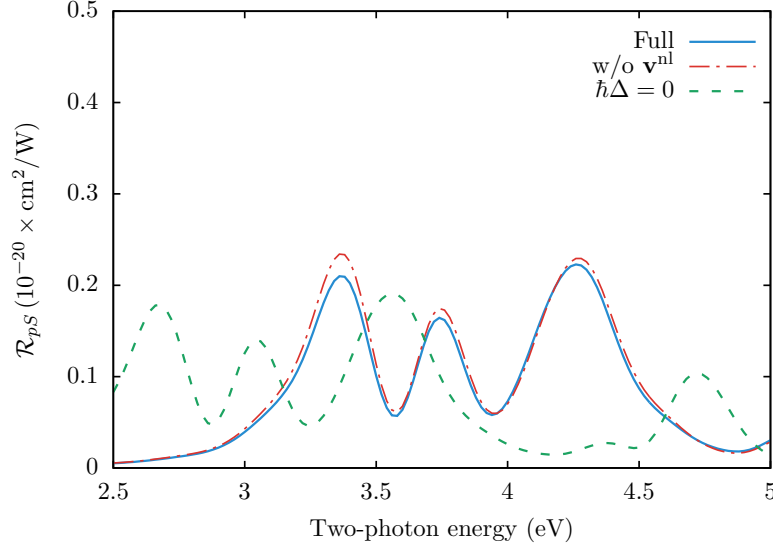


Figure 1.11: Calculated results for \mathcal{R}_{pS} for the different levels of approximation proposed in this article. All curves were calculated using the 3-layer model. We take $\theta = 65^\circ$ for this plot. See text for full details. All curves are broadened with $\sigma = 0.075$ eV.

sistent with the results reported in Ref. [32], where the exclusion of this term increases the intensity of the components of $\chi(-2\omega; \omega, \omega)$ by approximately 15% to 20%. We also notice that the E_1 peak is larger than the E_2 peak, contrasting with the experiment, where the E_1 peak is smaller than E_2 . Lastly, the thin solid line depicts the full calculation with a scissors value of $\hbar\Delta = 0$. We notice that the spectrum is almost rigidly redshifted as this H-saturated surface has no electronic surface states.[32] Thus, this demonstrates the importance of including the scissors correction to accurately reproduce the experimental spectrum. In summary, the inclusion of the contribution from the nonlocal part of the pseudopotentials and the scissors operator on top of the 3-layer model produces spectra with a lineshape and intensity that compare favorably with the experimental data.

1.4.2 Calculated \mathcal{R}_{sP} compared to experiment

Next, we analyze and compare the calculated \mathcal{R}_{sP} spectra with experimental data from Ref. [3]. We again adhere to the experimental setup by taking an angle of incidence $\theta = 65^\circ$ and an azimuthal angle $\phi = 30^\circ$. From Fig. 1.12, we can immediately appreciate that the overall intensity of \mathcal{R}_{sP} is one

order of magnitude lower than \mathcal{R}_{pS} . The experimental data is far noisier than in the other cases but we can still discern the E_1 and E_2 peaks. As with our previous comparisons, the 3-layer model is the closest match in both intensity and lineshape to the experimental spectrum. It produces a curve that is very close to the experimental intensity with good proportional heights for the calculated E_1 and E_2 peaks. In contrast, the 2-layer-vacuum model is 100 times more intense than experiment and produces an enlarged E_2 peak. The 2-layer-bulk model is ten times smaller with a very similar lineshape to the 3-layer model.

The differences between the 2-layer-vacuum and 2-layer-bulk models are not derived from Eq. (??), as the $\varepsilon_b(2\omega)$ does not change and the second term vanishes for this azimuthal angle of $\phi = 30$. However, Γ_{sP}^ℓ does cause a significant change in the intensity as there is an $\varepsilon_\ell(2\omega)$ term in the denominator. This will become $\varepsilon_v(2\omega) = 1$ for the 2-layer-vacuum model, and $\varepsilon_b(2\omega)$ in the bulk model. This accounts for the significant difference between the intensity of the two models, while the lineshape remains mostly consistent.

At higher energies, the theoretical curve is blueshifted as compared to the experiment. We consider that the likely explanation for this is the inclusion of the scissor operator, which does not adequately correct the transitions occurring at these higher energies. A full GW calculation would be well suited for this task, but is beyond the scope of this paper.

1.4.3 Calculated \mathcal{R}_{pP} compared to experiment

We present \mathcal{R}_{pP} compared to experimental data from Ref. [3] in Fig. 1.14. We note that peak position for the 3-layer model is similar to experiment with the overall intensity being only two times larger. The E_2 peak is blueshifted by around 0.3 eV, and the yield does not go to zero after 4.75 eV. The 2-layer-vacuum model produces a spectrum with peak positions that are close to the experiment, but are 40 times more intense. The calculated E_2 peak is similar, but the E_1 peak lacks the sharpness present in the experiment. The 2-layer-bulk model is very close to the lineshape of the 3-layer model, but with eight times less intensity. From Eq. (??), we see that \mathcal{R}_{pP} has several 2ω terms that will change between models; this will have a deep effect on the lineshape. Additionally, Γ_{pP}^ℓ also has $\varepsilon_\ell(2\omega)$ in the denominator, and so we have a significant difference in both lineshape and intensity between the 2-layer-vacuum and the other two models. Again, as in the previous sections for \mathcal{R}_{pS} and \mathcal{R}_{sP} , the 3-layer model is the closest in intensity to the experiment. Additionally, Ref. [31] shows that low temperature mea-

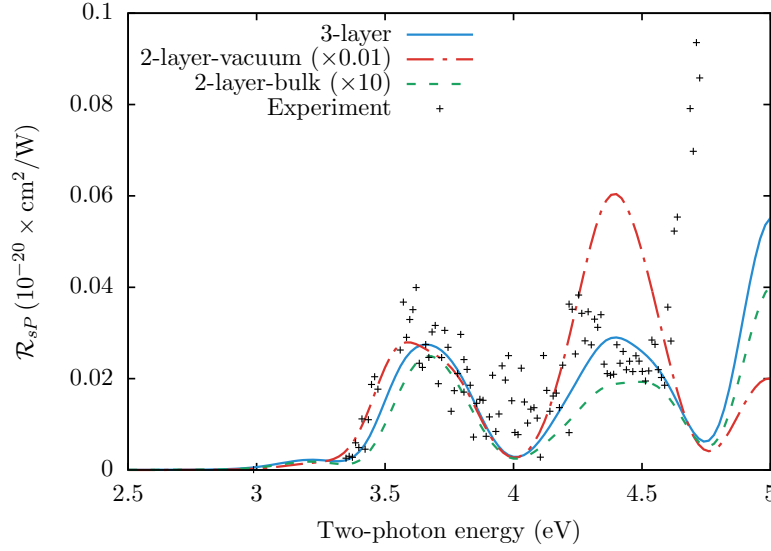


Figure 1.12: Comparison between theoretical models (see Table ??) and experiment for \mathcal{R}_{sP} , for $\theta = 65^\circ$. We use a scissors value of $\hbar\Delta = 0.7\text{ eV}$. All theoretical curves are broadened with $\sigma = 0.075\text{ eV}$. Experimental data taken from Ref. [3], measured at room temperature.

measurements of \mathcal{R}_{pP} will blueshift the spectrum away from room temperature measurements such as those shown in Figs. 1.14 and 1.15, and towards our theoretical results.

Reviewing Eq. (??), we see that \mathcal{R}_{pP} is by far the most involved calculation, since it includes all four nonzero components. In particular, $\chi_{\perp\perp\perp}$ and $\chi_{\parallel\parallel\perp}$ include out-of-plane incoming fields. These are affected by local field effects[24] that reveal the inhomogeneities in the material, which are by far more prevalent perpendicular to the surface than in the surface plane. This can be evidenced for Si, as Reflectance Anisotropy Spectroscopy (RAS) measurements are well described by *ab initio* calculations neglecting local field effects.[33, 34] It is therefore expected that the out-of-plane components will be more sensitive to the inclusion of local fields. These will not change the transition energies, only their relative weights of the resonant peaks,[24] but including these effects is challenging to compute,[35] and beyond the scope of this paper. We speculate that \mathcal{R}_{pP} requires the proper inclusion of these effects in order to accurately describe the experimental peaks.

In Fig. 1.15 we compare to Ref. [4]. The 3-layer model is, as before, close to the experiment in both peak position and intensity. Intensity is

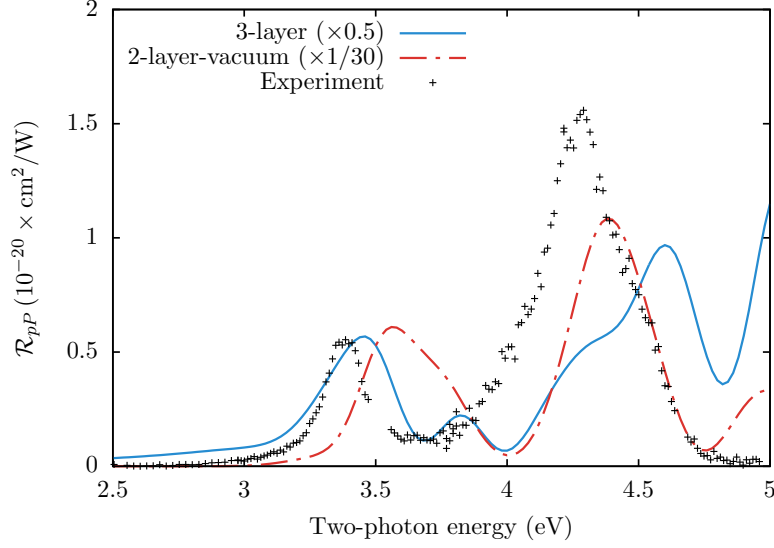


Figure 1.13: Comparison between theoretical models (see Table ??) and experiment for \mathcal{R}_{pP} , for $\theta = 65^\circ$. We use a scissors value of $\hbar\Delta = 0.7 \text{ eV}$. All theoretical curves are broadened with $\sigma = 0.075 \text{ eV}$. Experimental data taken from Ref. [3], measured at room temperature.

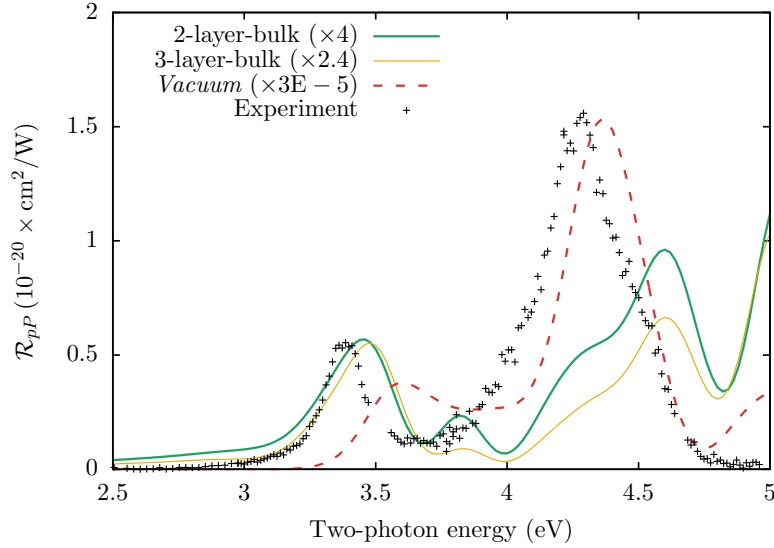


Figure 1.14: Other models.

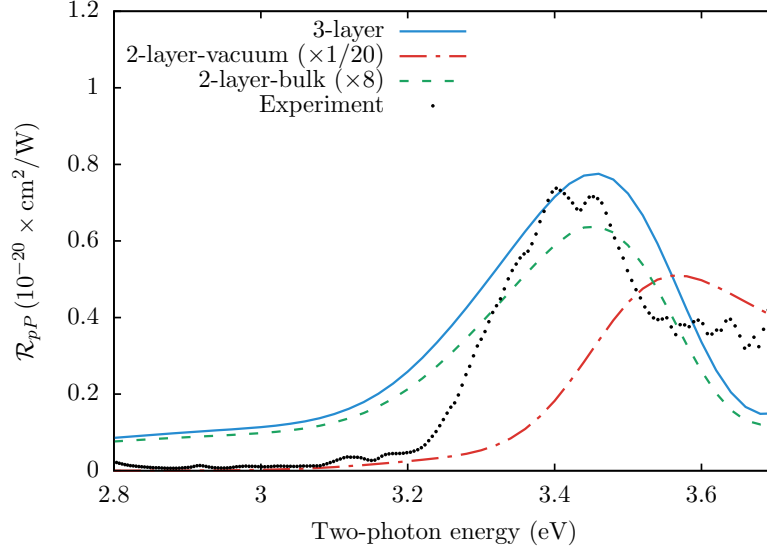


Figure 1.15: Comparison between theoretical models (see Table ??) and experiment for \mathcal{R}_{pP} , for $\theta = 45^\circ$. We use a scissors value of $\hbar\Delta = 0.7$ eV. All theoretical curves are broadened with $\sigma = 0.075$ eV. Experimental data taken from Ref. [4], measured at room temperature.

almost the same the experimental value. This provides a more compelling argument against the 2-layer-vacuum model than Fig. 1.14. The 2-layer-vacuum model is 20 times more intense and blueshifted by around 0.1 eV. As mentioned before, this surface is of very high quality with measurements taken shortly after surface preparation. As before, the 2-layer-bulk model is intermediate between the other two models in both intensity and lineshape. Under these conditions, the 3-layer model very accurately reproduces the E_1 peak over the 2-layer-vacuum and 2-layer-bulk models.

Lastly, for linear optics and SHG, GW transition energies are needed. Doing a Bethe-Salpeter calculation for SSHG will improve the position and the amplitude of the peaks, but is far beyond current capabilities.[36] We did not adjust the value of the scissors shift, as we want to keep our calculation at the *ab initio* level. We remark again that the choice of $\hbar\Delta = 0.7$ eV for the scissors shift comes from a GW calculation.[30] As explained in Fig. 1.11, the lack of surface states causes an almost rigid shift of the spectra by applying the scissors correction. We have checked that it is not possible to have a single scissors value that can reproduce the energy positions of both the E_1 and the E_2 peaks. Of course, the experimental temperature at which

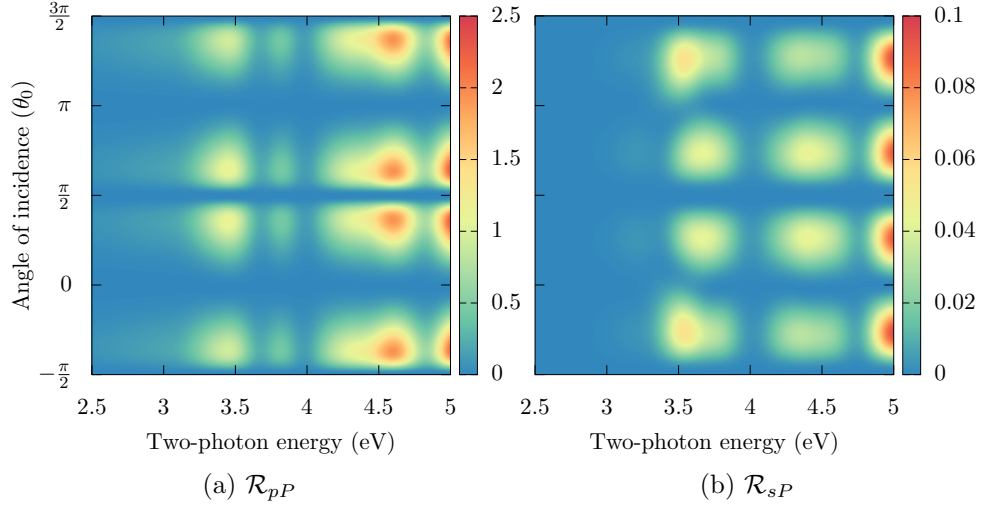


Figure 1.16: \mathcal{R} for outgoing P polarized fields, versus the angle of incidence (θ_0) for the Si(111)(1 \times 1):H surface. Both figures consider an azimuthal angle of $\phi = 45^\circ$. All curves are broadened with $\sigma = 0.075$ eV.

the spectra is measured should be taken into account in a more complete formulation. However, we have restricted our calculation to $T = 0$ K.

1.4.4 Calculating \mathcal{R}_{iF} including the effects of multiple reflections

We consider a Si(111)(1 \times 1):H surface as a test case for the three layer model and to study the effects that multiple reflections have on the SSHG radiation. This surface is well characterized experimentally,[4, 3, 2] and there has been success in reproducing these experimental results using the three layer model without multiple reflections.[?] The details of the *ab initio* calculation of χ_{ijk} are not needed for the following discussion, and are left for the reader in Ref. [?]. However, we mention that we apply a scissors shift of 0.7 eV to the theoretical spectra. In a first approximation, this includes the effects of the electronic many-body interactions within the independent particle approach for the *ab initio* calculation. This 0.7 eV value allows the SH resonant peaks to acquire their corresponding energy positions, and is calculated with what is known as a G_0W_0 calculation.[?] As mentioned in Sec. ??, we are interested in finding the thickness of the layer ℓ where $\chi_{ijk} \neq 0$. For this surface, we found well-converged results for a thickness of ~ 5 nm, that is equivalent to 24 atomic sheets of Si along the (111)

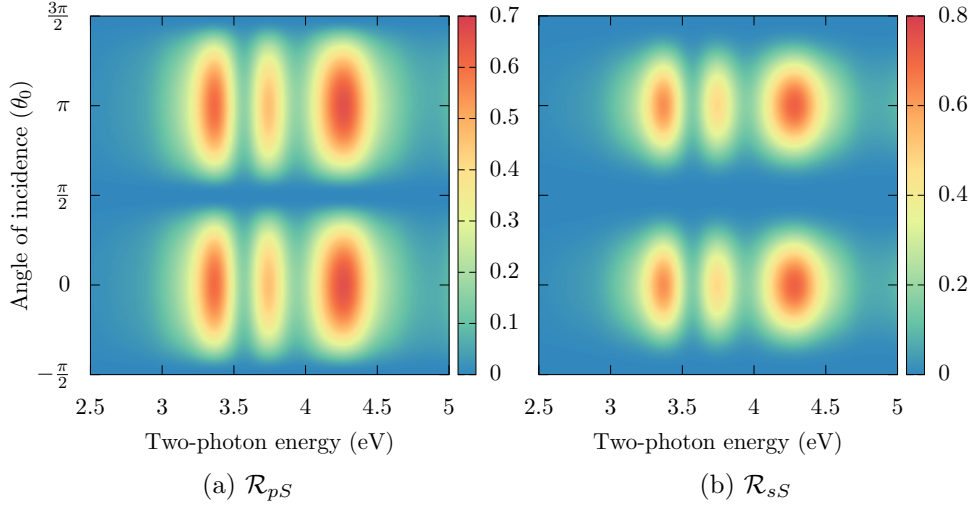


Figure 1.17: \mathcal{R} for outgoing S polarized fields, versus the angle of incidence (θ_0) for the $Si(111)(1\times 1):H$ surface. Both figures consider an azimuthal angle of $\phi = 45^\circ$. All curves are broadened with $\sigma = 0.075$ eV.

direction. As this represents only the upper half of the slab, we find it reasonable to choose the thickness of the layer ℓ to be between $d \sim 5 - 10$ nm. This corresponds to a half-slab comprised of 24 to 48 atomic layers to get well-converged values of χ_{ijk} .

In Fig. ??, we compare the theoretical results for the SSHG yield with the experimental results from Ref. [3]. We mention that the experimental results were produced with an angle of incidence of $\theta = 65^\circ$, and an azimuthal angle of $\phi = 30^\circ$, which eliminates the contribution from χ_{xxx} from Eq. (??). First, we note that the experimental spectrum shows two very well defined resonances which come from electronic transitions from the valence to the conduction bands around the well known $E_1 \sim 3.4$ eV and $E_2 \sim 4.3$ eV critical points of Si.[37] As can be seen, the theoretical results reproduce the features of the spectrum, although we see that the E_2 peak is blueshifted by around 0.3 eV. Here we focus on the SSHG yield itself rather than on the physics that lead to such a blueshifted theoretical spectrum. The interested reader can refer to Ref. [?] for those details.

All curves in this figure that include multiple reflections consider $d = 10$ nm. We compare the theoretical SSHG yield for $d_2 = 0$ nm and $d_2 = 10$ nm, with the SSHG yield that neglects multiple reflections. When $d_2 = 0$ nm, we have placed the polarization sheet at the bottom of the layer region. This

minimizes the effect of the multiple reflections, and thus the curve is very similar to the three layer model that neglects multiple reflections entirely. When $d_2 = 10$ nm, the polarization sheet is placed at the top of the layer region. This maximizes the effect of the multiple reflections and therefore leads to the largest yield. We also notice that the average value obtained by using \bar{R}_i^M (Eq. (??)) is intermediate between $d_2 = 0$ and $d_2 = 10$ nm, as expected. This is very similar to selecting $d_2 = d/2$, which can be interpreted as placing the nonlinear polarization sheet $\mathbf{P}(\mathbf{r}, t)$ at the middle of layer ℓ . It is important to remark that these enhancements are larger for E_2 than for E_1 . This can be understood from the fact that the corresponding λ_0 for E_1 is larger than that of E_2 . From Eqs. (??), (??), and (??), we see that the phase shifts are larger for E_2 than for E_1 , producing a larger enhancement of the SSHG yield at E_2 from the multiple reflections. As the phase shifts grow with d , so does the enhancement caused by the multiple reflections. We have verified that the effects of the multiple reflections from the linear field are significantly smaller than those of the SH field. This is clear since the phase shift of Eq. (??) is not only a factor of 2 smaller than that of Eqs. (??) and (??), but also $w_\ell < W_\ell$.

From this figure, it becomes evident that the inclusion of multiple reflections is crucial to obtain a better agreement between the theoretical SSHG yield and the experimental spectrum. This is particularly true for larger energies, such as E_2 , as λ_0 becomes smaller and the multiple reflection effects become more noticeable. The selected value for $d \ll \lambda_0$, that comes naturally from the *ab initio* calculation of χ_{ijk} is thus very reasonable in order to model a thin surface layer below the vacuum region where the nonlinear SH conversion takes place.

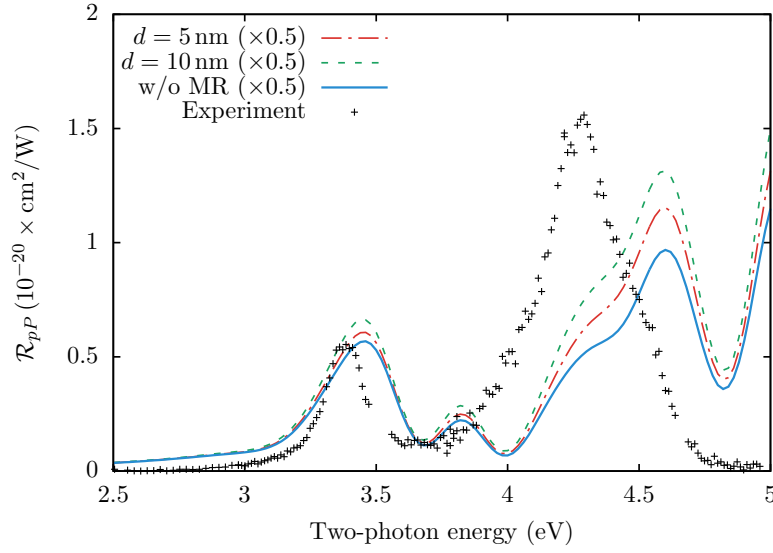


Figure 1.18: Comparison between theoretical models (see Table ??) and experiment for \mathcal{R}_{pP} , for $\theta = 45^\circ$. We use a scissors value of $\hbar\Delta = 0.7 \text{ eV}$. All theoretical curves are broadened with $\sigma = 0.075 \text{ eV}$. Experimental data taken from Ref. [4], measured at room temperature.

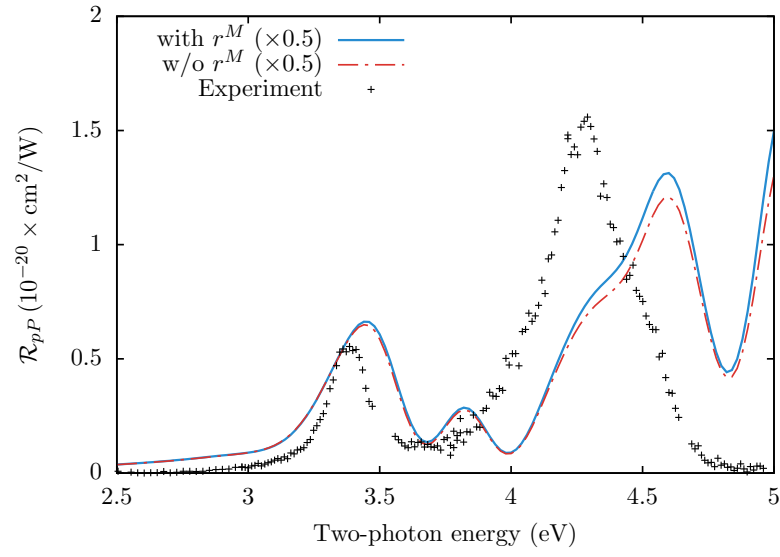


Figure 1.19: Comparison between theoretical models (see Table ??) and experiment for \mathcal{R}_{pP} , for $\theta = 45^\circ$. We use a scissors value of $\hbar\Delta = 0.7$ eV. All theoretical curves are broadened with $\sigma = 0.075$ eV. Experimental data taken from Ref. [4], measured at room temperature.

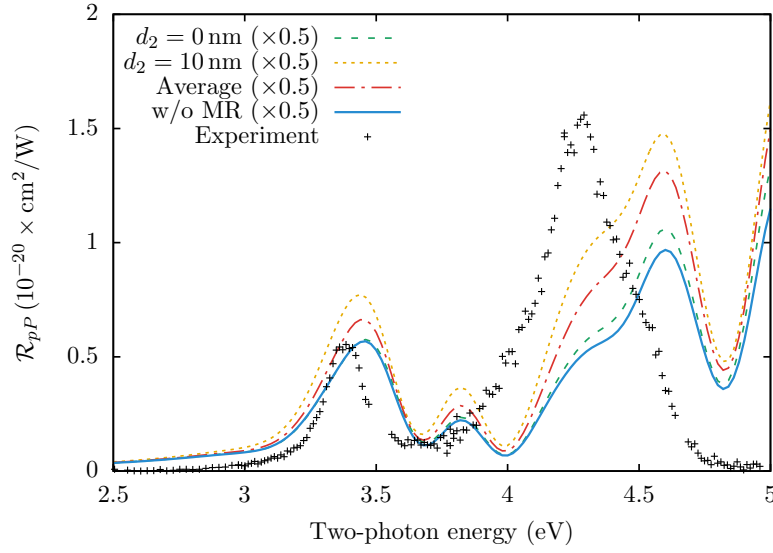


Figure 1.20: Comparison between theoretical models (see Table ??) and experiment for \mathcal{R}_{pP} , for $\theta = 45^\circ$. We use a scissors value of $\hbar\Delta = 0.7 \text{ eV}$. All theoretical curves are broadened with $\sigma = 0.075 \text{ eV}$. Experimental data taken from Ref. [4], measured at room temperature.

Bibliography

- [1] U. Höfer. Nonlinear optical investigations of the dynamics of hydrogen interaction with silicon surfaces. *Appl. Phys. A*, 63(6):533–547, December 1996.
- [2] S. Bergfeld, B. Braunschweig, and W. Daum. Nonlinear Optical Spectroscopy of Suboxides at Oxidized Si(111) Interfaces. *Phys. Rev. Lett.*, 93(9):097402, August 2004.
- [3] J. E. Mejía, B. S. Mendoza, M. Palummo, G. Onida, R. Del Sole, S. Bergfeld, and W. Daum. Surface second-harmonic generation from si (111)(1x1) h: Theory versus experiment. *Phys. Rev. B*, 66(19):195329, 2002.
- [4] S. A. Mitchell, M. Mehendale, D. M. Villeneuve, and R. Boukherroub. Second harmonic generation spectroscopy of chemically modified Si(1 1 1) surfaces. *Surf. Sci.*, 488(3):367–378, August 2001.
- [5] The half-slab layer extends to the middle of the vacuum region between consecutive (front-back or back-front) surfaces of the repeated super cell scheme.
- [6] X. Gonze, B. Amadon, P. . M. Anglade, J. . M. Beuken, F. Bottin, P. Boulanger, F. Bruneval, D. Caliste, R. Caracas, M. Cote, T. Deutsch, L. Genovese, Ph. Ghosez, M. Giantomassi, S. Goedecker, D. R. Hamann, P. Hermet, F. Jollet, G. Jomard, S. Leroux, M. Mancini, S. Mazevet, M. J. T. Oliveira, G. Onida, Y. Pouillon, T. Rangel, G. . M. Rignanese, D. Sangalli, R. Shaltaf, M. Torrent, M. J. Verstraete, G. Zerah, and J. W. Zwanziger. ABINIT: First-principles approach to material and nanosystem properties. *Comput. Phys. Commun.*, 180(12):2582–2615, December 2009.

- [7] The ABINIT code is a common project of the Université Catholique de Louvain, Corning Incorporated, and other contributors (URL <http://www.abinit.org>).
- [8] N. Troullier and J. L. Martins. Efficient pseudopotentials for plane-wave calculations. *Phys. Rev. B*, 43(3):1993–2006, January 1991.
- [9] L. Kleinman and D. M. Bylander. Efficacious form for model pseudopotentials. *Phys. Rev. Lett.*, 48(20):1425–1428, 1982.
- [10] V. Olevano, L. Reining, and F. Sottile. <http://dp-code.org>.
- [11] L. Caramella, C. Hogan, G. Onida, and R. Del Sole. High-resolution electron energy loss spectra of reconstructed si(100) surfaces: First-principles study. *Phys. Rev. B*, 79:155447, Apr 2009.
- [12] B. S. Mendoza, F. Nastos, N. Arzate, and J. Sipe. Layer-by-layer analysis of the linear optical response of clean and hydrogenated si(100) surfaces. *Phys. Rev. B*, 74(7):075318, 2006.
- [13] For bulk calculations schemes of the SH susceptibility tensor beyond the independent particle approximation, see Refs. [23, 22, 21, 38, 39, 40, 41, 42].
- [14] F. Nastos, B. Olejnik, K. Schwarz, and J. E. Sipe. Scissors implementation within length-gauge formulations of the frequency-dependent non-linear optical response of semiconductors. *Phys. Rev. B*, 72(4):045223, 2005.
- [15] Valérie Vénierd, E. Luppi, and H. Hübener. unpublished.
- [16] M. Rohlfing, P. Krüger, and J. Pollmann. Efficient scheme for GW quasiparticle band-structure calculations with applications to bulk si and to the si(001)-(2x1) surface. *Phys. Rev. B*, 52(3):1905–1917, July 1995.
- [17] P. García-González and R. W. Godby. GW self-energy calculations for surfaces and interfaces. *Comput. Phys. Commun.*, 137(1):108–122, June 2001.
- [18] Eleonora Luppi, Hans-Christian Weissker, Sandro Bottaro, Sottile Francesco, Valérie Vénierd, Lucia Reining, and Giovanni Onida. Accuracy of the pseudopotential approximation in *ab initio* theoretical spectroscopies. *Phys. Rev. B*, 78:245124, 2008.

- [19] R. Asahi, W. Mannstadt, and A. J. Freeman. Screened-exchange lda methods for films and superlattices with applications to the si(100)2x1 surface and inasinsb superlattices. *Phys. Rev. B*, 62:2552, 2000.
- [20] J. Cabellos, B. Mendoza, M. Escobar, F. Nastos, and J. Sipe. Effects of nonlocality on second-harmonic generation in bulk semiconductors. *Phys. Rev. B*, 80(15):155205, 2009.
- [21] E. Luppi, H. Hübener, and V. Véniard. Ab initio second-order nonlinear optics in solids: Second-harmonic generation spectroscopy from time-dependent density-functional theory. *Phys. Rev. B*, 82:235201, 2010.
- [22] R. Leitsmann, W. Schmidt, P. Hahn, and F. Bechstedt. Second-harmonic polarizability including electron-hole attraction from band-structure theory. *Phys. Rev. B*, 71(19):195209, 2005.
- [23] B. Adolph and F. Bechstedt. Influence of crystal structure and quasiparticle effects on second-harmonic generation: Silicon carbide polytypes. *Phys. Rev. B*, 62:1706, 2000.
- [24] Nicolas Tancogne-Dejean. *Ab initio description of second-harmonic generation from crystal surfaces*. PhD thesis, Ecole polytechnique, September 2015.
- [25] E. Kaxiras and J. D. Joannopoulos. Hydrogenation of semiconductor surfaces: Si and Ge (111). *Phys. Rev. B*, 37(15):8842–8848, May 1988.
- [26] F. Jona, W. A. Thompson, and P. M. Marcus. Experimental determination of the atomic structure of a H-terminated Si(111) surface. *Phys. Rev. B*, 52(11):8226–8230, September 1995.
- [27] D. R. Alfonso, C. Noguez, D. A. Drabold, and S. E. Ulloa. First-principles studies of hydrogenated Si(111)-7x7. *Phys. Rev. B*, 54(11):8028–8032, September 1996.
- [28] F. Cargnoni, C. Gatti, E. May, and D. Narducci. Geometrical reconstructions and electronic relaxations of silicon surfaces. I. An electron density topological study of H-covered and clean Si(111)(1x1) surfaces. *J. Chem. Phys.*, 112(2):887–899, January 2000.
- [29] R. C. Weast, M. J. Astle, and W. H. Beyer. *CRC handbook of chemistry and physics*, volume 69. CRC press Boca Raton, FL, 1988.

- [30] Y. Li and G. Galli. Electronic and spectroscopic properties of the hydrogen-terminated Si(111) surface from ab initio calculations. *Phys. Rev. B*, 82(4):045321, July 2010.
- [31] J. I. Dadap, Z. Xu, X. F. Hu, M. C. Downer, N. M. Russell, J. G. Ekerdt, and O. A. Aktsipetrov. Second-harmonic spectroscopy of a Si (001) surface during calibrated variations in temperature and hydrogen coverage. *Phys. Rev. B*, 56(20):13367, 1997.
- [32] S. M. Anderson, N. Tancogne-Dejean, B. S. Mendoza, and V. Vénard. Theory of surface second-harmonic generation for semiconductors including effects of nonlocal operators. *Phys. Rev. B*, 91(7):075302, February 2015.
- [33] M. Palummo, G. Onida, R. Del Sole, and B. S. Mendoza. Ab initio optical properties of Si(100). *Phys. Rev. B*, 60(4):2522–2527, July 1999.
- [34] K. Gaál-Nagy, A. Incze, G. Onida, Y. Borensztein, N. Witkowski, O. Pluchery, F. Fuchs, F. Bechstedt, and R. Del Sole. Optical spectra and microscopic structure of the oxidized Si(100) surface: Combined in situ optical experiments and first principles calculations. *Phys. Rev. B*, 79(4):045312, January 2009.
- [35] N. Tancogne-Dejean, C. Giorgetti, and V. Vénard. Optical properties of surfaces with supercell *ab initio* calculations: Local-field effects. *Phys. Rev. B*, 92(24):245308, July 2015.
- [36] The size of the excitonic Hamiltonian scales as $(N_k^3 \times N_v \times N_c)^2$, where N_k is the total number of \mathbf{k} -points, and N_v and N_c are the number of valence and conduction states, respectively. For these values, the size of the Hamiltonian for the Si(111)(1×1):H surface of this article would be over 1 petabyte, which far exceeds conventional computing capabilities.
- [37] P. Yu and M. Cardona. *Fundamentals of Semiconductors: Physics and Materials Properties*. Springer Science & Business Media, third edition, March 2005.
- [38] E. Luppi, H. Hübener, and V. Vénard. Communications: Ab initio second-order nonlinear optics in solids. *J. Chem. Phys.*, 132(24):241104, 2010.
- [39] H. Hübener, E. Luppi, and V. Vénard. Ab initio calculation of many-body effects on the second-harmonic generation spectra of hexagonal sic polytypes. *Phys. Rev. B*, 83:115205, 2011.

- [40] Mads L. Trolle, Gotthard Seifert, and Thomas G. Pedersen. Theory of excitonic second-harmonic generation in monolayer MoS₂. *Phys. Rev. B*, 89(23):235410, June 2014.
- [41] C. Attaccalite and M. Grüning. Nonlinear optics from an ab initio approach by means of the dynamical berry phase: Application to second- and third-harmonic generation in semiconductors. *Phys. Rev. B*, 88:235113, 2013.
- [42] M. Grüning and C. Attaccalite. Second harmonic generation in *h*-bn and mos₂ monolayers: Role of electron-hole interaction. *Phys. Rev. B*, 89:081102, 2014.